FAST EVALUATION OF PASSIVE SAFETY IN NEAR-FIELD OPERATIONS

Bruce L. Barbour and Dr. Kevin K. Schroeder
Virginia Tech, Blacksburg, VA 24060

Abstract—This paper introduces a novel closed-form method for evaluating passive safety (PS) in near-field spacecraft operations. Drawing on the geometric insights provided by relative orbital elements (ROEs), the paper develops a safety criteria that capture both keep-out volumes and general out-of-plane relative motion. Additionally, a binary search algorithm is employed to deliver fast and quantifiable safety metrics, thereby providing improved situational awareness. The method is demonstrated through an application in orbit reconfiguration of the Iridium NEXT constellation, identifying collision risks across three rendezvous strategies. This research contributes to the advancement of on-orbit support for real-time PS analysis, particularly in applications critical to NASA's mission, for more autonomous spacecraft operations in the evolving space environment.

Introduction

Due to a recent surge in space activities, a proliferation in artificial satellites and operational spacecraft, and a flourishing commercial space industry, ensuring safety for future autonomous spacecraft has emerged as a unique challenge. Although advances in tracking and cataloging orbiting objects[1–3] have been significant, real-time onboard capabilities still lag behind growing safety demands. While strict collision avoidance protocols are enforced from the ground, there is a clear need for more capable onboard systems[4–6].

Modern collision risk mitigation strategies rely on passively safe relative motion concepts in both the far field and near field[7–9]. Traditionally, safeguarding spacecraft has involved defining geometric regions centered on the client spacecraft—known as Keep-Out Volumes (KOV) or Keep-Out Zones (KOZ)—modeled as ellipsoids with dimensions based on navigation uncertainties[10]. Evaluating passive safety (PS) through relative motion dynamics typically requires computing the state at every point[9, 11, 12]. In contrast, recent work has leveraged relative orbital elements (ROEs) to model relative motion, which can greatly reduce the computational burden of point-wise analysis, thus enabling more real-time capability. This approach has been successfully applied to distributed space systems (DSS) such as GRACE[13], TanDEM-X/TerraSAR-X[14], and PRISMA[15], where enforcing relative eccentricity and inclination (E/I) vector separation via ROEs has proven effective for mission-safe operations.

Prior work on PS assessment has examined reachable sets[16] and used differences in orbital elements along with the concept of the KOV to generate avoidance sets[17]. Although robust, computing reachable sets for non-Keplerian dynamics is complex and time-consuming. In DSS applications, E/I ROEs are frequently used for PS analysis[18–22]; however, applying the E/I assumption in close-proximity operations introduces limitations[22, 21]. To relax this assumption, Sullivan[19] developed closed-form solutions that geometrically characterize an elliptical relative motion as a function of the E/I ROEs. Building on these insights, Chernick[23] represented the relative motion with a bounding box model, and later, Guffanti[20] incorporated these ellipse parameters into PS applications while retaining the E/I assumption without fully examining the ellipse. More recently, Borelli et al.[22] advanced this framework by modeling the relative motion as a closed polytope with a finite number of boundary constraints. Although solutions beyond the E/I assumption remain relatively sparse, more general approaches with high computational efficiency and accuracy are attainable.

This paper introduces a novel closed-form method in support of real-time PS analysis for ballistic relative motion in the near field. The approach builds on the E/I vector separation concept while achieving higher dimensionality and preserving computational efficiency. Compared to previous works, this method simplifies PS checking through exact ellipse modeling and employs a rapid search algorithm to quantify PS. The proposed method is applied to a realistic scenario involving the constellation orbit reconfiguration of the Iridium NEXT constellation using NORAD two-line element sets (TLE) data, detailing representative transfer trajectories for reconfiguration and using the PS method to assess collision risk. The study demonstrates the method's effectiveness in capturing the dynamics accurately and highlights its potential as a constraint in trajectory planning.

Astrodynamics of Relative Motion

This section provides a brief background of relative motion between two spacecraft, commonly referred to as the chief and the deputy. The chief travels along a ballistic trajectory and establishes the reference orbit, while the deputy can modify its relative path to the chief using controlled thrust.

2.1 Reference Frame

The Radial/In-track/Cross-track (RIC) frame is a locally defined Cartesian coordinate system that is typically centered on the chief spacecraft. Using this reference frame provides simpler modeling of the dynamics because the axes are more aligned with the principal directions of motion compared to other systems. Its $\hat{R}$-axis (radial) is aligned with the position vector in the Earth-centered inertial (ECI) frame that points from the center of the primary body to the chief, $\hat{C}$-axis (cross-track) is coincident with the orbital angular momentum vector, and $\hat{I}$-axis (in-track) is the vector normal to the $\hat{R}$- and $\hat{C}$-axes, completing the right-handed triad.

2.2 Relative Orbital Elements

The quasi-nonsingular relative orbital elements (ROE) in Eq. (1), derived in D'Amico et al.[18], provide key geometric insights into relative motion. The subscript d refers to the deputy spacecraft, while quantities without a subscript pertain to the chief. These geometric states remain well-behaved for circular chief orbits ($e = 0$) but become singular for equatorial orbits ($i = 0$). In this formulation, the separation of the relative eccentricity vector $\delta\vec{e}$ and the relative inclination vector $\delta\vec{i}$ is central. ROEs are nonlinear functions of the chief's and deputy's absolute orbital elements—specifically, the semi-major axis (a), eccentricity (e), inclination (i), right ascension of the ascending node (Ω), argument of periapsis (ω), and mean anomaly (M). Here, the mean anomaly M replaces the true anomaly ν (which are approximately equal in near-circular orbits). Unlike the Hill-Clohessy-Wiltshire (HCW) equations, which neglect eccentricity effects, the ROE method retains this information through $\delta\vec{e}$, resulting in improved accuracy[24]. Although the six ROE states in Eq. (1) are dimensionless, scaling them by the chief's semi-major axis a gives them physical significance.

$$\delta\vec{\alpha} = \begin{pmatrix} \delta a \\ \delta\lambda \\ \delta e_x \\ \delta e_y \\ \delta i_x \\ \delta i_y \end{pmatrix} = \begin{pmatrix} \delta a \\ \delta\lambda \\ \delta e\cos\varphi \\ \delta e\sin\varphi \\ \delta i\cos\vartheta \\ \delta i\sin\vartheta \end{pmatrix} \tag{1}$$

$$\triangleq \begin{pmatrix} (a_d - a)/a \\ (M_d - M) + (\omega_d - \omega) + (\Omega_d - \Omega)\cos i \\ e_d\cos\omega_d - e\cos\omega \\ e_d\sin\omega_d - e\sin\omega \\ i_d - i \\ (\Omega_d - \Omega)\sin i \end{pmatrix} \tag{2}$$

Here, δa represents the relative semi-major axis, and $\delta\lambda$ the relative mean longitude. The pairs $(\delta e_x, \delta e_y)$ and $(\delta i_x, \delta i_y)$ are the components of the relative eccentricity and inclination vectors, with their magnitudes given by $\delta e = \sqrt{\delta {e_x}^2 + \delta {e_y}^2}$ and $\delta i = \sqrt{\delta {i_x}^2 + \delta {i_y}^2}$, respectively. Their phase angles φ (relative argument of perigee) and ϑ (relative ascending node) are computed as:

$$\varphi = \textbf{atan2}(\delta e_y, \delta e_x), \quad \vartheta = \textbf{atan2}(\delta i_y, \delta i_x) \tag{3}$$

Methodology

3.1 Out-of-Plane Relative Motion

When modeling in-plane relative motion, two distinct trajectories can emerge when introducing a radial offset. In Fig. 1.A, a positive nonzero $a\delta a$ induces a spiral-like trajectory that drifts in the $-\hat{I}$ direction. On the other hand, Fig. 1.B illustrates an RI-plane trajectory with zero $a\delta a$. This RI-plane trajectory maintains $a\delta\lambda$ through zero drift, exhibiting periodic motion around a relative orbit center. In this case, an in-track dimension can be more feasibly defined due to the closed shape. Similarly, Fig. 2 demonstrates that ROEs can also directly characterize the geometry of a near-circular RC-plane trajectory. However, the in-track drift caused by a nonzero $a\delta a$ does not affect the RC-plane in the same manner as in the RI-plane. This is due to the RC-plane being orthogonal to the in-track direction. Thus, the RC-plane relative trajectories represented in both Fig. 2.A and Fig. 2.B exhibit identical closed shapes, despite introducing a non-zero radial offset. This fundamental characteristic of out-of-plane motion enables the establishment of a consistent PS check.

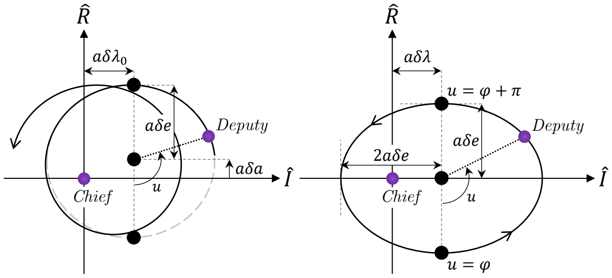

(a) (b)

Fig. 1: Sketch of an RI-plane trajectory: (a) with radial offset; (b) without radial offset.

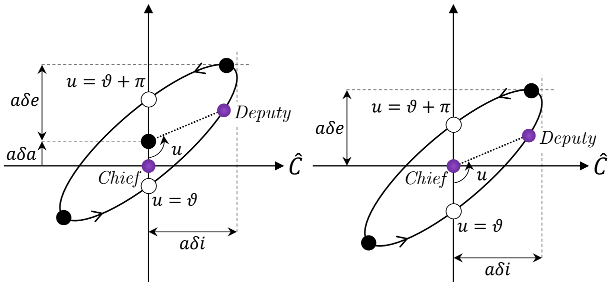

(a) (b)

Fig. 2: Sketch of an RC-plane trajectory: (a) with radial offset; (b) without radial offset.

3.2 Mapped Ellipse Envelopes

With the analytical solutions provided by the HCW equations, it is possible to trace an ellipse in the RC-plane. The transformation from ROEs to relative Cartesian is achieved through a first-order equivalence between ROEs and the integration constants of the HCW equations[25]. Since the ROEs are derived from the absolute orbital elements, the resulting linearized states accurately describe the relative spacecraft motion for a near-circular chief. Equation (4) supplies the transformation for direct ROE-HCW mapping of the RC-plane components[19].

$$\begin{aligned}\begin{pmatrix}\delta x^R\\ \delta x^C\end{pmatrix} &= \begin{bmatrix}-a\,\delta e_x & -a\,\delta e_y\\ -a\,\delta i_y & a\,\delta i_x\end{bmatrix}\begin{pmatrix}\cos u\\ \sin u\end{pmatrix} + \begin{pmatrix}a\,\delta a\\ 0\end{pmatrix}\\ &\triangleq \underline{\Gamma}\begin{pmatrix}\cos u\\ \sin u\end{pmatrix} + \begin{pmatrix}a\,\delta a\\ 0\end{pmatrix}\end{aligned} \tag{4}$$

The relative trajectory projected onto the RC-plane, defined as the envelope Θ_{RC}, can be represented by a geometrically rotated ellipse with a radial offset along $\hat{R}$, as depicted in Fig. 3. Using the mapping in Eq. (4), the semi-axes of the ellipse can be analytically determined through matrix decomposition. Since $\underline{\Gamma}$ is not inherently symmetric, singular value decomposition (SVD) is more suitable than eigendecomposition to ensure orthogonality. Thus, the semi-axes and orientation of Θ_{RC} can be derived using the SVD of $\underline{\Gamma}$,

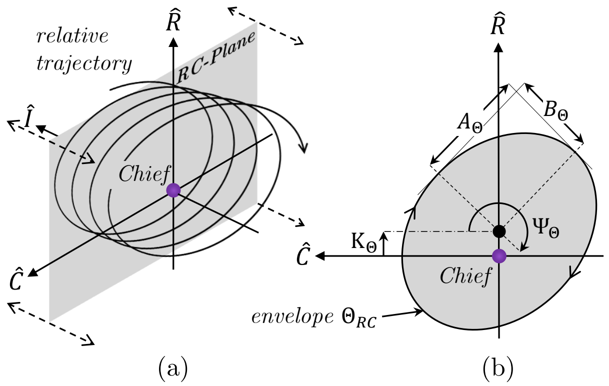

Fig. 3: Relative trajectory projected onto the RC-plane, modeled as an envelope with defined ellipse parameters.

$$(A_\Theta, B_\Theta) = \frac{a}{\sqrt{2}} + \Bigg[\delta e^2 + \delta i^2 \pm \sqrt{\delta e^4 + \delta i^4 - 2\,\delta e^2\,\delta i^2\,\cos\Big(2(\varphi - \vartheta)\Big)}\,\Bigg]^{\frac{1}{2}} \tag{5}$$

$$\Psi_\Theta = \frac{1}{2}\,\textbf{atan2}\big(2\delta e\delta i\sin(\varphi - \vartheta),\ \delta e^2 - \delta i^2\big) \tag{6}$$

Finally, K_Θ can be deduced as $a\delta a$ from Eq. (4). These four quantities collectively characterize Θ_{RC} by its size, shape, orientation, and radial offset. Although the trajectory is accurately modeled, it still depends on the inherent ROE formulation's small-angle assumption for out-of-plane motion. Consequently, the ellipse model remains valid when the separation between the two spacecraft is negligible compared to the chief's semi-major axis[26].

Similar to the relative trajectory, the KOV can also be projected onto the RC-plane to form the envelope $\mathcal{S}_{RC}$ as illustrated in Fig. 4. Though, in contrast, this envelope $\mathcal{S}_{RC}$ does not have any offset nor rotation. Therefore, the semi-axes of $\mathcal{S}_{RC}$, denoted as $A_\mathcal{S}$ and $B_\mathcal{S}$, are coincident with the RC-plane coordinate axes.

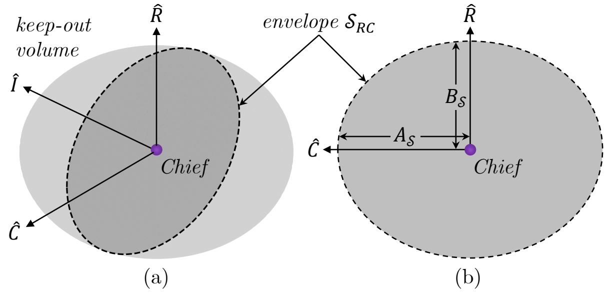

Fig. 4: Projection of a KOV onto the RC-plane, modeled as an envelope with defined semi-axes.

3.3 Passive Safety Criteria

Although various factors may influence PS[10], PS within a defined safety horizon can be achieved when both Necessary Condition A (NCA) and Necessary Condition B (NCB) are met, ensuring that the near-field relative trajectory remains outside the KOV. To verify this, NCA uses a bounding box constraint that divides into two sub-conditions based on whether the center of Θ_{RC} lies inside or outside the $\hat{R}$-boundary of $\mathcal{S}_{RC}$. Formally, NCA is defined as follows:

- **NCA.I:** The center of Θ_{RC}, which lies along the unit vector $\hat{R}$, shall be located beyond the boundary of $\mathcal{S}_{RC}$, expressed as:
$$\textbf{abs}(K_\Theta) - B_\mathcal{S} > 0 \tag{7}$$
- **NCA.II:** The envelope $\mathcal{S}_{RC}$ must not entirely contain Θ_{RC}. For this condition to hold, the semi-axes of Θ_{RC} must exceed those of $\mathcal{S}_{RC}$. Equation (8) represents a generalization of the semi-axes of $\mathcal{S}_{RC}$ to accommodate for different keep-out configurations:
$$\begin{cases} A_\Theta > \max(A_\mathcal{S},\, B_\mathcal{S})\\ B_\Theta > \min(A_\mathcal{S},\, B_\mathcal{S})\end{cases} \tag{8}$$

Next, NCB ensures that the ellipse envelopes do not intersect. Although the absence of intersections might imply safety, PS is not guaranteed unless NCA is also met. This condition can be formally expressed as:

- **NCB:** The envelopes Θ_{RC} and $\mathcal{S}_{RC}$ shall not intersect nor share any common points, in other words,

$$\Theta_{RC} \cap \mathcal{S}_{RC} = \emptyset \tag{9}$$

It is essential to verify both NCA and NCB simultaneously. For example, if Θ_{RC} is entirely within $\mathcal{S}_{RC}$, no intersections may be detected even though PS is clearly violated. Similarly, even when if Θ_{RC} is principally larger than $\mathcal{S}_{RC}$, orientation or offset can cause intersections. An advantage of the interdependent necessary conditions is that NCA serves as an initial filter for unsafe trajectories, while NCB enables a more flexible assessment using precise ellipse modeling.

Verification of NCA can be performed analytically using Eqs. (7) and (8). In contrast, evaluating Eq. (9) to satisfy NCB is analytically more complex, as discussed in the next subsection. To minimize runtime, it is efficient to first check NCA because it can be computed quickly using the bounding box model. If the conditions in Eqs. (7) and (8) are not met, the trajectory can immediately be classified as unsafe. Only when NCA is satisfied should one proceed to evaluate NCB using Eq. (9). Figure 5 depicts a high-level algorithm flowchart that adopts this strategy.

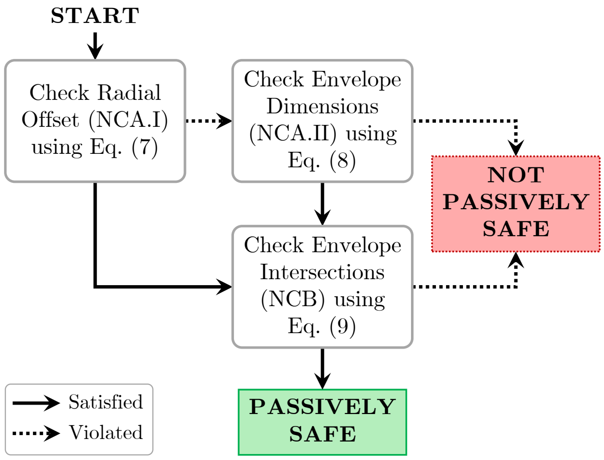

Fig. 5: High-level flowchart for evaluating ROE-based passive safety.

3.4 Transforming Envelopes To Exact Ellipses

To check for NCB, it is necessary to represent the envelopes Θ_{RC} and $\mathcal{S}_{RC}$ using differentiable functions. The equation for a general ellipse can be expressed as follows:

$$\begin{aligned} 0 = -1 \; &+ \frac{\left[x \cos \Psi + (y - K) \sin \Psi\right]^2}{A^2} \\ &+ \frac{\left[x \sin \Psi - (y - K) \cos \Psi\right]^2}{B^2} \end{aligned} \tag{10}$$

In this general equation, the parameters A, B, Ψ, and K can be tailored to each envelope expressed in Figs. 3 and 4. Due to the small-angle assumption, there is no x-offset term, and the KOV excludes a cross-track offset. By performing operations such as completing the square, expanding, and rearranging Eq. (10), the general ellipse equation can be reformulated as Eq. (11) to model Θ_{RC} as a second-degree bivariate polynomial:

$$\begin{aligned} &F_\Theta\left(x, y; A_\Theta, B_\Theta, \Psi_\Theta, K_\Theta\right) \\ &\quad = b_5 x^2 + b_4 xy + b_3 y^2 + b_2 x + b_1 y + b_0 \end{aligned} \tag{11}$$

Here, the coefficients of F_Θ, denoted as b_k, are functions of the ellipse parameters of Θ_{RC} as follows:

$$\begin{aligned} b_5 &= \frac{\cos^2\left(\Psi_\Theta\right)}{A_\Theta^2} + \frac{\sin^2\left(\Psi_\Theta\right)}{B_\Theta^2} \\ b_4 &= \frac{\sin\left(2\Psi_\Theta\right)}{A_\Theta^2} - \frac{\sin\left(2\Psi_\Theta\right)}{B_\Theta^2} \\ b_3 &= \frac{\sin^2\left(\Psi_\Theta\right)}{A_\Theta^2} + \frac{\cos^2\left(\Psi_\Theta\right)}{B_\Theta^2} \\ b_2 &= -K_\Theta b_4 \\ b_1 &= -2K_\Theta b_3 \\ b_0 &= -1 + K_\Theta^2 b_3 \end{aligned} \tag{12}$$

The coefficients b_k indicate that only the parameters $A_\Theta, B_\Theta, \Psi_\Theta$, and K_Θ are pertinent, which corresponds with Θ_{RC} as shown in Fig. 3. Consequently, the condition $F_\Theta = 0$ represents the locus of the relative trajectory envelope.

Similarly, Eq. (13) captures the envelope $\mathcal{S}_{RC}$ in Fig. 4, where the condition $F_\mathcal{S} = 0$ defines the locus of the keep-out envelope. The simpler standard ellipse equation (without rotation and offset) is used, as ellipse orientation and radial offset are not considered, eliminating the need for the variable terms xy, x, and y.

$$F_\mathcal{S}\left(x, y; A_\mathcal{S}, B_\mathcal{S}\right) = c_5 x^2 + c_3 y^2 + c_0 \tag{13}$$

Here, the coefficients c_5, c_3 and c_0 become only functions of the principal components of $\mathcal{S}_{RC}$ as given:

$$c_5 = \frac{1}{A_\mathcal{S}^2}, \qquad c_3 = \frac{1}{B_\mathcal{S}^2}, \qquad c_0 = -1 \tag{14}$$

3.5 Solving Exact Ellipse Intersections

To preserve the two-dimensional information of Eqs. (11) and (13) while simplifying the problem to a univariate form, a recently developed approach uses the complex plane through the variable $z = x + i\ y$. Instead of directly examining the relationship between Θ_{RC} and $\mathcal{S}_{RC}$, the keep-out envelope $\mathcal{S}_{RC}$ undergoes a transformation to the unit circle, resulting in $\mathcal{S}_{RC}^U$. The same transformation applied to $\mathcal{S}_{RC}^U$ is subsequently used on Θ_{RC} to derive Θ_{RC}^U, aligning both within the transformed $(RC)^U$-plane. It is assumed throughout that Θ_{RC} and $\mathcal{S}_{RC}$ are non-degenerate ellipses. Figure 6

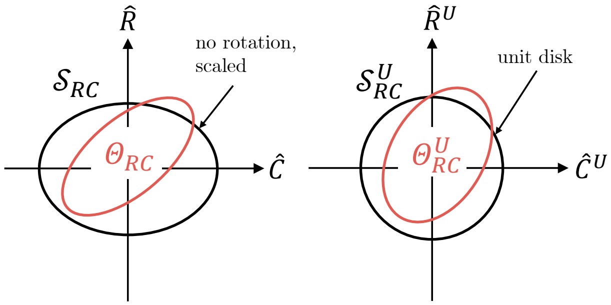

(a) (b)

Fig. 6: Visualization of the unit disk transformation into a transformed $(RC)^U$-plane through coordinate scaling: (a) pre-transformation; (b) post-transformation.

illustrates the unit disk transformation for a standard case.

As $\mathcal{S}_{RC}$ is inherently aligned with the unit circle, only its semi-axes require scaling to match the unit circle's uniform radius of 1. By applying the same transformation to Θ_{RC}, the resulting envelope Θ^U_{RC} is characterized by the coefficient matrix H, as shown below:

$$H = \begin{bmatrix} h_5 & \frac{1}{2}h_4 & \frac{1}{2}h_2 \\ \frac{1}{2}h_4 & h_3 & \frac{1}{2}h_1 \\ \frac{1}{2}h_2 & \frac{1}{2}h_1 & h_0 \end{bmatrix} \triangleq \begin{bmatrix} b_5c_5 & \frac{1}{2}b_4\sqrt{c_5}\sqrt{c_3} & \frac{1}{2}b_2\sqrt{c_5} \\ \frac{1}{2}b_4\sqrt{c_5}\sqrt{c_3} & b_3c_3 & \frac{1}{2}b_1\sqrt{c_3} \\ \frac{1}{2}b_2\sqrt{c_5} & \frac{1}{2}b_1\sqrt{c_3} & b_0 \end{bmatrix} \tag{15}$$

The entries in H correspond to the coefficients of the ellipse equation for Θ^U_{RC}, analogous to Eq. (11). Applying a Fourier series transforms the ellipse equation into a univariate representation in the complex plane for Θ^U_{RC}, expressed using $z = e^{i\xi}$ as follows:

$$\begin{aligned} P(z) = {} & \tfrac{1}{2}(h_5 - h_3 - h_4 i)z^4 + (h_2 - h_1 i)z^3 \\ & + (h_5 + h_3 + 2b_0)z^2 + (h_2 + h_1 i)z \\ & + \tfrac{1}{2}(h_5 - h_3 + h_4 i) \end{aligned} \tag{16}$$

Here, Eq. (16) exhibits a conjugate-palindromic structure, implying self-inversion and symmetry of roots with respect to the unit circle. According to Cohn's theorem[27], the reciprocal polynomial $P^*(z)$ can be expressed as:

$$\begin{aligned} P^*(z) = {} & \tfrac{1}{2}(h_5 - h_3 + h_4 i)z^4 + (h_2 + h_1 i)z^3 \\ & + (h_5 + h_3 + 2b_0)z^2 + (h_2 - h_1 i)z \\ & + \tfrac{1}{2}(h_5 - h_3 - h_4 i) \end{aligned} \tag{17}$$

By taking the derivative of $P^*(z)$, the quartic polynomial is reduced to the cubic polynomial $p(z)$. Per Cohn's theorem, the derivative $p(z)$ of the reciprocal polynomial has the same number of roots inside the open unit disk as $P(z)$. This simplifies finding the roots, as solving a cubic polynomial analytically is more straightforward than solving a quartic. Thus, the critical equation to solve is:

$$\begin{aligned} p(z) = {} & \underbrace{(h_2 + h_1 i)}_{\mathbf{p_3}} z^3 + \underbrace{2(h_5 + h_3 + 2h_0)}_{\mathbf{p_2}} z^2 \\ & + \underbrace{3(h_2 - h_1 i)}_{\mathbf{p_1}} z + \underbrace{2(h_5 - h_3 - h_4 i)}_{\mathbf{p_0}} \end{aligned} \tag{18}$$

The envelope Θ^U_{RC} does not intersect the unit circle *if and only if* $p(z)$ has exactly two roots z inside the unit disk. Mathematically, this condition can be expressed through the following criterion:

$$\sum_{k=0}^{2} \{|z_k - 1| < 0\} \geq 2 \tag{19}$$

Here, the summation evaluates the number of roots z_k that satisfy the condition $|z_k - 1| < 0$, where $|z_k - 1|$ represents the distance of the roots from the boundary of the unit disk. If at least two roots lie within the disk, it confirms that the envelope does not intersect the unit circle. Due to the variability of envelope parameters, multiple intersection scenarios may arise. These scenarios can be classified into cases involving cubic roots, quadratic roots, or single/infinite roots. The first two cases indicate a potential absence of intersection, whereas single or infinite roots fail to satisfy Eq. (19) and thus violate the condition.

3.5.1 Cubic Roots

Given that $p(z)$ may have complex coefficients, particularly when $h_1 \neq 0$ (for p_3, p_1) and $h_4 \neq 0$ (for p_0), the polynomial cannot be solved using standard methods for real coefficients. To address this, a general solution derived from Cardano's formula[28] is applied, offering a robust and effective approach for solving cubic polynomials with both real and complex coefficients.

Using the derived cubic polynomial $p(z)$, define:

$$\Delta_0 = p_2^2 - 3p_3p_1, \quad \Delta_1 = 2p_2^3 - 9p_3p_2p_1 + 27p_3^2p_0 \tag{20}$$

and let:

$$\mathcal{C} = \sqrt[3]{\frac{\Delta_1 \pm \sqrt{\Delta_1^2 - 4\Delta_0^3}}{2}} \tag{21}$$

The three roots of $p(z)$ are given by:

$$z_k = -\frac{1}{3p_3}\left(p_2 + \mathcal{I}^k\mathcal{C} + \frac{\Delta_0}{\mathcal{I}^k\mathcal{C}}\right), \quad k \in \{0, 1, 2\}, \tag{22}$$

where $\mathcal{I} = \frac{-1+\sqrt{-3}}{2}$ represents the cube roots of unity. When $\mathcal{C} \approx 0$, Eq. (22) may result in a singularity due to $\mathcal{C}$ appearing in the denominator of the third term. This issue can arise when the semi-axes of both envelopes are represented using very small values. To mitigate this, enforcing a small minimum tolerance such as 10^{-12}

for $\mathcal{C}$ can resolve the issue, preventing a zero-division error while preserving accuracy. Naturally, the choice of tolerance should be carefully considered, as smaller tolerances result in a lower impact from the introduced approximation.

3.5.2 Quadratic Roots

In cases where $p_3 = 0$, Eq. (18) simplifies to a quadratic polynomial:

$$p(z) = p_2 z^2 + p_1 z + p_0 \tag{23}$$

with discriminant:

$$\Delta = p_1^2 - 4p_2 p_0 \tag{24}$$

The two roots of the quadratic equation are then given by:

$$z_{0,1} = \frac{-p_1 \pm \sqrt{\Delta}}{2p_2} \tag{25}$$

In the unit disk approach, setting $K_\Theta = 0$ and $\Psi_\Theta = 0$ often leads to this quadratic form, which corresponds to bounded (anti) parallel alignment of $\delta\vec{e}$ and $\delta\vec{i}$.

3.5.3 Single/Infinite Roots

When $p_3 = p_2 = 0$, there is only a single root, given by $z_0 = -p_0/p_1$. However, having only one root does not meet the criterion for no intersections, as at least two roots are required, thereby resolving to an intersection. If $p_1 = 0$ as well, the equation results in infinitely many roots, which indicates a perfect overlap of the envelopes. In this case, all roots z_k rest on the boundary of the unit disk and are equal to unity.

3.6 Passive Safety Quantification

Since the PS method produces a binary outcome, a search algorithm can be effectivly used to determine the extent of PS. In this work, the binary search was chosen due to its time complexity of $\mathcal{O}(\log n)$ based on the "divide-and-conquer" approach[29]. This algorithm identifies the transition point at which the method hovers between safe/unsafe, which reflects the inherent ambiguity when near the KOV boundary. This point is found by iteratively inflating or compressing the envelope $\mathcal{S}_{RC}$ with a scale factor β until an exact intersection is reached, while maintaining a constant Θ_{RC}. The scale factor at this transition, denoted as β^*, distinguishes it from the iterative variable. Thus, β^* represents the fraction of the KOV that the trajectory occupies. Naturally, if $\beta^* \leq 1$, it indicates that Θ_{RC} intersects with $\mathcal{S}_{RC}$.

Orbit Reconfiguration Study

4.1 Problem Setup and Assumptions

This study aims to showcase the proposed PS method by applying it to a real-world example of constellation orbit reconfiguration. As satellite constellations expand, implementing effective reconfiguration strategies is essential for collision avoidance and overall mission success. Here, the PS method is employed in a practical rendezvous scenario, highlighting its ability to manage relative motion dynamics and the perturbations typical in space operations.

The reconfiguration analysis was conducted using a case study based on NORAD TLE data from the Iridium NEXT constellation. This constellation adopts a Walker Star Pattern in the 85°: 66/6/2 configuration, comprising 66 satellites across 6 orbital planes. As shown in Fig. 7, the scenario is divided into three stages:

- Stage I: Initial orbit is operational without any disruption.
- Stage II: A satellite node ceases operations, causing an intra-orbit disconnect.
- Stage III: Spare satellite is deployed to the vacant slot to re-establish the network.

In the diagram, white circles indicate operational satellites, while the purple circle represents the spare satellite, located slightly ahead of an operational one. In Stage II, the disrupted satellite is shown as a red circle marked with an 'x'. By Stage III, it is assumed that the disrupted satellite has been removed, leaving an open slot. This study focuses on Stage III, where the PS method is applied to assess and design potential rendezvous trajectory options for repositioning the spare satellite into the vacant slot.

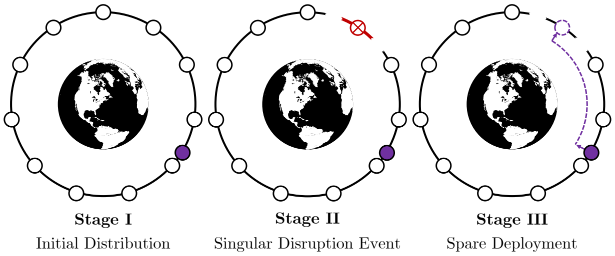
Stage I Initial Distribution

Stage II Singular Disruption Event

Stage III Spare Deployment

Fig. 7: Illustration of the example three-stage scenario.

Satellite dynamics are propagated using SGP4, with TLEs at the initial epoch used throughout. Although TLE propagation carries an error of about 1–3 km/day[30], this does not affect the study's focus. The TLEs are converted from mean to osculating elements and then propagated to a common epoch. All satellites except for the spare follow an unforced, ballistic trajectory, while the spare uses three degree of freedom controlled thrust, starting at its initial location and then approaching the vacant slot. Additionally, the satellite dynamics are assumed known, and the spare can acquire the osculating orbital elements of any satellite within a 100-km range. For the Iridium NEXT constellation, this range (approximately 1.5% of the 7160 km orbital radius) meets the small separation assumption required for relative motion modeling. These orbital elements are used to compute ROEs and generate trajectory envelopes for PS assessment. The prescribed KOV from Table I is applied to all satellites; if the spare's RC-plane trajectory avoids intersecting any KOV, it is considered PS with respect to out-of-plane separation.

TABLE I: KOV dimensions defined for each satellite.

Radial [m]	In-track [m]	Cross-track [m]
5000	5000	5000

4.2 Relative Motion Design

As depicted in Stage III of Fig. 7, the spare satellite is situated three slots behind the Target. To reach the Target slot, it must perform a maneuver that adjusts its orbital energy so that it can drift into position. Although the spare can drift either prograde or retrograde, minimizing the time to re-establish the network is paramount; thus, the focus is on the direction that offers the shortest path. For clarity, the satellites in the prograde direction are identified as follows:

- **Satellite 2**: The next satellite directly in front of the spare.
- **Satellite 3**: Positioned ahead of Satellite 2 and just behind the Target slot.
- **Target**: The Target position for the spare's reconfiguration.

The spare's relative trajectory is determined by its state after the maneuver in relation to Satellite 2, which in turn influences its subsequent motion with respect to other satellites. Because these satellite states are derived from TLE data and are thus affected by perturbations, differences in their absolute orbital elements lead to varying relative motions. Although the initial relative motion with Satellite 2 might naturally serve as a design reference, this study instead uses the final relative motion at the Target slot to establish the initial trajectory design. This design uses a single transfer trajectory to ensure that the spare rendezvouses with the Target after the prescribed TOF.

Three transfer trajectory types were evaluated for repositioning the spare into the Target slot. While not an exhaustive list of rendezvous strategies, the selected approaches are described below:

1) **Coplanar Elliptic Transfer Orbit (CPET)**: The spare is inserted into a slightly lower orbit with a minor eccentricity adjustment to increase its mean motion and "catch up" to the Target. Although this approach may have safety concerns at apoapsis, it remains common for maneuver phasing.
2) **Coplanar Circular Transfer Orbit (CPCT)**: A burn at periapsis circularizes the orbit from the initial elliptical transfer, creating a significant radial buffer between the spare, the Target, and other satellites, which yields high PS.
3) **Walking Safety Ellipse (WSE)**: This trajectory emphasizes out-of-plane separation. By leveraging a small orbital energy difference to achieve a large combined radial/cross-track separation with in-track drift, it achieves a PS V-bar approach.

Results and Discussion

Table II presents the mean orbital elements derived from the TLEs of the four satellites, as well as the corresponding mean elements for the spare along the three transfer trajectories. The satellite names serve purely as identifiers and do not denote operational designations. Note that the transfer trajectories are not optimized but are provided to exemplify different transfer types and facilitate a PS assessment.

Figures 8, 9, and 10 depict the out-of-plane relative motion in the RC-plane. The left and middle subplots depict the spare's drift toward Satellites 2 and 3, respectively——starting at a 100-km encounter, reaching closest approach, then moving beyond 100 km. The right subplots illustrate the spare approaching the Target slot for final repositioning. The light gray line represents the simulated trajectory, the orange dashed line defines the elliptical envelope of the ROE states at the beginning of the encounter, and the blue dashed line shows the envelope at zero in-track separation ($\delta r^I = 0$). The orange/blue 'x' markers indicate the center points of the envelopes. In particular, the spare fails to maintain a safe out-of-plane separation during elliptic transfer. In a Walker Star constellation with ideal two-body dynamics, a CPET would exhibit no cross-track separation, oscillating solely along the $\hat{R}$-direction and returning to the initial orbital radius at apoapsis. This behavior might induce a collision risk due to insufficient separation and potential crossing with the KOV along the R-bar. However, initial perturbations induce changes in eccentricity and inclination, forming the elliptical shapes observed.

The spare encounter with Satellite 3 (middle subplot in Fig. 8) reveals almost double the cross-track separation compared to Satellite 2, and even more relative to the Target, attributable to the greater initial inclination difference indicated in Table II. Although the envelope shows maximum cross-track ranges of 5–15 km, its center point lies along the KOV boundary, creating a substantial region of intersection and an unsafe trajectory. No differences were observed between the two PS checks (approximately 3.5 hours apart), and the full transfer trajectory extended over 17.6 days.

While CPET does not yield a PS rendezvous, the circular approach ensures high PS during each encounter. Since CPCT builds on the elliptic transfer, the envelopes in Figs. 8 and 9 resemble each other along their semi-major axes. However, differences in the semi-minor axis, a negative radial offset, and a clockwise rotation bring the CPCT envelope nearly into tangency with the lower KOV boundary. These factors afford CPCT

TABLE II: Mean elements of the four satellite TLEs and different spare transfer trajectories along the focused orbit.

ID	i [deg]	Ω [deg]	e	ω [deg]	M [deg]	n [rev/day]
Satellite 2	86.3917	257.8589	0.0002	86.6944	150.0623	14.3422
Satellite 3	86.3915	257.8092	0.0002	79.3105	190.1738	14.3422
Target	86.3918	257.8562	0.0002	82.7514	219.4631	14.3422
Spare	86.3919	257.9236	0.0002	88.0523	118.4088	14.3422
Spare (CPET)	86.3919	257.9236	0.0007	206.4511	0.0000	14.3575
Spare (CPCT)	86.3919	257.9090	0.0002	26.4233	0.0000	14.3728
Spare (WSE)	86.3946	257.9364	0.0054	88.1865	138.4088	14.3572

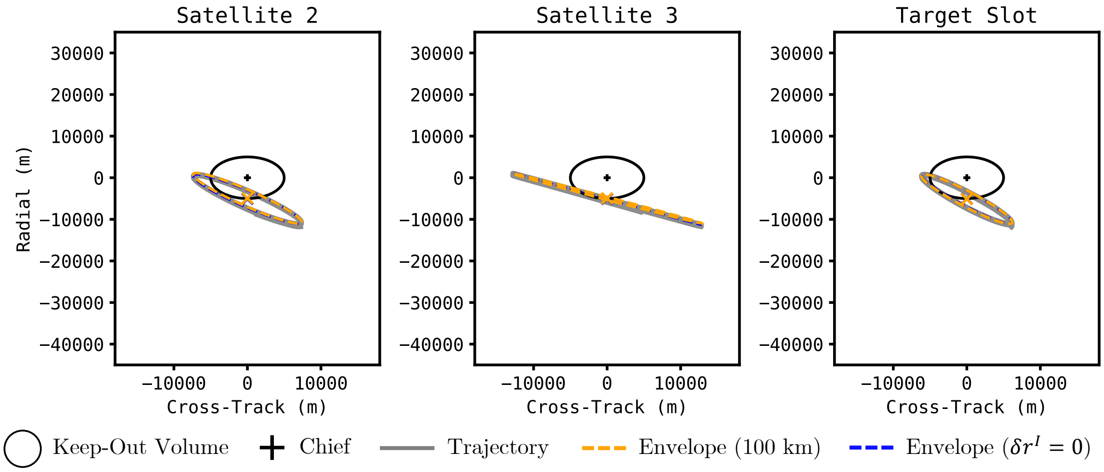

Fig. 8: RC-plane trajectory of the spare within 100-km approach of each satellite during CPCT.

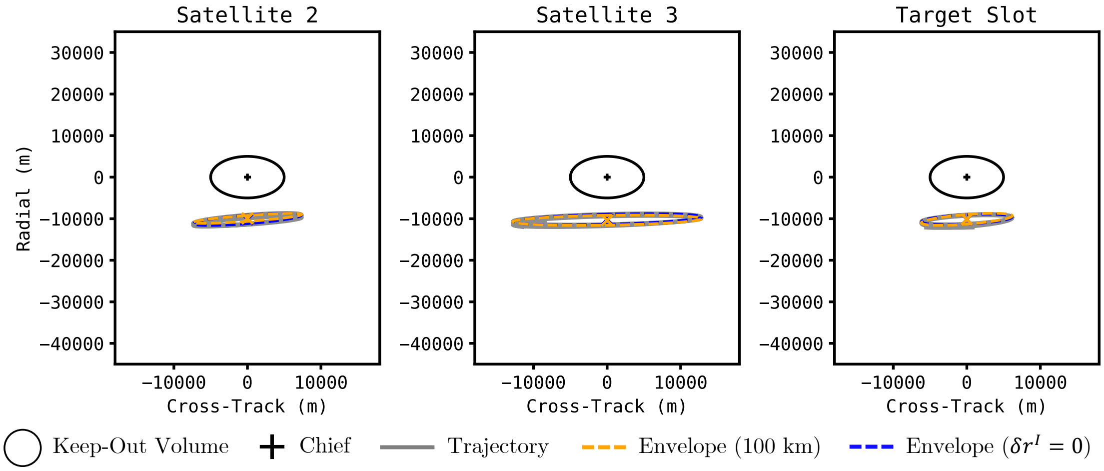

Fig. 9: RC-plane trajectory of the spare within 100-km approach of each satellite during CPET.

a substantial radial offset, with the closest approach providing margins of roughly 5000 m. This resulted in a higher drift rate leading to a 8.7-day TOF. With an ellipse tilt angle close to zero, the cross-track separation essentially equals the ellipse semi-major axis, while its semi-minor axis represents the radial offset along the center. Minor variations between the PS check at 100 km and zero in-track (around 2 hours apart) reflect additional perturbation effects.

A significant advantage of the proposed PS method is

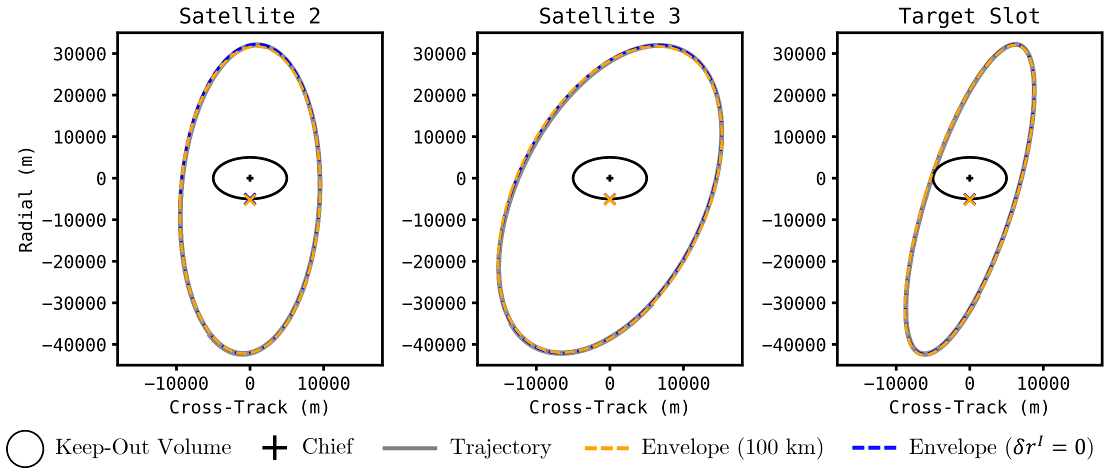

Fig. 10: RC-plane trajectory of the spare within 100-km approach of each satellite during WSE.

that it does not require the envelope to completely encapsulate the KOV—a constraint that would be violated by each trajectory shown in Fig. 8 and 9 if using the polytope approach[22]. Even with near-degenerate ellipses (e.g., the middle subplot of Fig. 8), decomposing the RC-plane motion into the envelope effectively captures the dynamics.

Compared with coplanar approaches, the WSE trajectory leverages natural out-of-plane motion to achieve PS. As shown in Fig. 10, the RC-plane trajectory fully encloses the KOV, ensuring safe radial and cross-track separations during all encounters. Similar to CPET, the PS checks occur approximately 3.5 hours apart. Traditionally, a WSE is designed as a slow approach with modest radial offset[10], but the initial WSE design (see Table III), defined via ROEs relative to the Target's TLE, employs a high walk rate resulting in a TOF of roughly 15.3 days, positioning it between CPET and CPCT.

TABLE III: Initial WSE design relative to Target's TLE at initial epoch.

$a\delta a$ [km]	$a\delta e_x$ [km]	$a\delta e_y$ [km]	$a\delta i_x$ [km]	$a\delta i_y$ [km]
-5.0000	1.3960	39.9756	0.3490	9.9939

To counteract the required radial offset from the high walk rate, the WSE trajectory adopts larger separations (up to 10 km in cross-track and 40 km radially) thus accommodating greater in-track uncertainty. By fully encapsulating the KOV (and the Target slot), the trajectory enables a full-view inspection of both in-plane and out-of-plane dynamics. This is particularly advantageous for pre-inspection procedures aimed at detecting potential debris hazards, even though a slower walk rate might be preferable for detailed inspections. Such considerations are more pertinent for future missions, as most current communication satellites lack the necessary sensor payloads.

TABLE IV: β^* values for the RC-plane envelope within 100-km approach of each satellite for the three transfer trajectories.

Trajectory	ID	β^* (100 km)	β^* ($\delta r^I = 0$)
CPET	Satellite 2	0.4553	0.4797
	Satellite 3	0.8367	0.8947
	Target	0.4644	0.4675
CPCT	Satellite 2	1.8286	1.8133
	Satellite 3	1.8347	1.7859
	Target	1.7859	1.7981
WSE	Satellite 2	1.8469	1.8469
	Satellite 3	2.4756	2.4573
	Target	1.0412	1.0412

Table IV provides the quantified PS solutions for the two PS checks at each satellite encounter across the three transfer options. These results span from largely unsafe to largely safe conditions. While the WSE trajectory delivers comparable PS for Satellite 2 and significantly higher safety for Satellite 3, its β^* near the Target decreases considerably, yielding only marginal PS. Notably, the β^* for WSE remains nearly unchanged between the PS checks for Satellite 2 and the Target and varies only nominally for Satellite 3. In contrast, CPCT maintains consistently high PS from a robust radial offset, whereas CPET fails to achieve PS, with β^* values falling below the threshold of 1. Convergence to a β^* value was reached within just 15 iterations (at a tolerance of 10^{-3}) over a β range of [0, 50], with computation times around 5 μs per iteration. These results showcase the effectiveness of the proposed PS method in evaluating a range of relative rendezvous trajectories. Although further research could refine the overall methodology, the current approach shows significant promise not only in supporting rendezvous operations but also in conducting PS checks on debris and incorporating the PS method as an optimization constraint in trajectory planning.

Conclusions and Future Work

Evaluation of PS in near-field spacecraft operations is critical for ensuring collision-free trajectories and operational reliability, particularly as mission complexity deepens due to an ever-increasing satellite population. This paper demonstrates that integrating a closed-form ellipse intersection method with the geometric insights from ROEs creates a robust safety criteria that effectively captures both avoidance regions and out-of-plane dynamics. Furthermore, employing a binary search algorithm enables rapid PS quantification, thereby improving situational awareness and supporting real-time analyses for autonomous operations. As the space environment continually evolves, this approach shows significant potential for advancing trajectory planning and collision mitigation strategies. Future research into analytical solutions for quantified PS could enhance this methodology even further, ultimately contributing to safer and more efficient operations in alignment with NASA's mission and the broader interests of the space community.

Acknowledgements

The authors would like to thank the Virginia Tech and Virginia Space Grant Consortium (VSGC) for their generous financial support of this research and for the opportunity to contribute to NASA's mission in advancing space technology.

Works Cited

[1] C. Harris, D. J. Thomas, J. Kadan, K. K. Schroeder, and J. T. Black, "Expanding the space surveillance network with space-based sensors using metaheuristic optimization techniques," *2021 Advanced Maui Optical and Space Surveillance Technologies*, 2021.

[2] C. Frueh, "Sensor tasking for multi-sensor space object surveillance," *2017 European Conference on Space Debris*, 2017.

[3] Y. He, L. Xing, Y. Chen, W. Pedrycz, L. Wang, and G. Wu, "A generic markov decision process model and reinforcement learning method for scheduling agile earth observation satellites," *IEEE Transactions on Systems, Man, and Cybernetics: Systems*, vol. 52, no. 3, pp. 1463–1474, 2022.

[4] A. D. Wan, P. J. Braspenning, and G. A. Vreeswijk, "Limits to ground control in autonomous spacecraft," *Telematics and Informatics*, vol. 12, 1997.

[5] J. A. Starek, B. Açıkmeşe, I. A. Nesnas, and M. Pavone, *Spacecraft Autonomy Challenges for Next-Generation Space Missions*. Springer, 2015, pp. 1–48.

[6] G. J. Cancro, *APL Spacecraft Autonomy: Then, Now, and Tomorrow*. Applied Physics Laboratory, 2010, pp. 226–233.

[7] B. J. Naasz, "Safety ellipse motion with coarse sun angle optimization." https://core.ac.uk/download/pdf/10516198.pdf: 595 Flight Mechanics Symposium, 2005.

[8] D. S. Koons, C. Schreiber, F. Acevedo, and M. Sechrist, "Risk mitigation approach to commercial resupply to the international space station," *Fourth Annual International Association for the Advancement of Space*, 2010.

[9] A. W. B. Jr., E. R. Burnett, and S. Bieniawski, "Chance-constrained, drift-safe guidance for spacecraft rendezvous," *2023 AAS/AIAA Astrodynamics Specialist Conference*, 2023.

[10] M. A. Vavrina, C. E. Skelton, K. D. Deweese, B. J. Naasz, D. E. Gaylor, and C. D'Souza, "Safe rendezvous trajectory design for the restore-l mission," *2019 AAS/AIAA Space Flight Mechanics Meeting*, vol. 168, pp. 3649–3668, 2019.

[11] M. Goggin, "Rendezvous mission risk reduction through passively safe orbital rendezvous," *2019 Space Symposium, Technical Track*, 2019.

[12] N. Chan and S. Mitra, "Verifying safety of an autonomous spacecraft rendezvous mission," *4th International Workshop on Applied Verification of Continuous and Hybrid Systems*, vol. 48, pp. 20–32, 2017.

[13] O. Montenbruck, M. Kirschner, S. D'Amico, and S. Bettadpur, "E/i-vector separation for safe switching of the grace formation," *IEEE Spectrum*, 2006.

[14] M. Zink and et. al., "The tandem-x mission concept," *2006 IEEE International Symposium on Geoscience and Remote Sensing*, 2006.

[15] E. Gill, S. D'Amico, and O. Montenbruck, "Autonomous formation flying for the prisma mission," *Journal of Spacecraft and Rockets*, vol. 44, no. 3, 2007.

[16] M. Holzinger and D. Scheeres, "Applied reachability for space situational awareness and safety in spacecraft proximity operations," *AIAA Guidance, Navigation, and Control Conference*, 2009.

[17] D. Aguilar-Marsillach and M. J. Holzinger, "Passively safe spacecraft motion using reachable sets and orbital element differences," *Journal of Spacecraft and Rockets*, vol. 60, no. 5, pp. 1597–1613, 2023.

[18] S. D'Amico and O. Montenbruck, "Proximity operations of formation-flying spacecraft using an eccentricity/inclination vector separation," *Journal of Guidance, Control, and Dynamics*, vol. 29, no. 3, pp. 554–563, 2006.

[19] J. Sullivan, A. W. Koenig, and S. D'Amico, "Improved maneuver-free approach to angles-only navigation for space rendezvous," *2016 AAS/AIAA Astrodynamics Specialist Conference*, pp. 9–10, 2016.

[20] T. Guffanti and S. D'Amico, "Passively safe and robust multi-agent optimal control with application to distributed space systems," *Journal of Guidance, Control, and Dynamics*, vol. 46, no. 8, pp. 1448–1469, 2023.

[21] J. Wang, C. Zhang, and J. Zhang, "Analytical solution of satellite formation impulsive reconfiguration considering passive safety constraints," *Aerospace Science and Technology*, vol. 119, 2021.

[22] G. Borelli, G. Gaias, and C. Colombo, "Safe guidance scheme for proximity operations forced motion," *Journal of Guidance, Control, and Dynamics*, vol. 48, no. 2, pp. 340–357, 2025.

[23] M. Chernick, "Optimal impulsive control of spacecraft relative motion," Ph.D. dissertation, Stanford University, 2021.

[24] J. Sullivan, S. Grimberg, and S. D'Amico, "Comprehensive survey and assessment of spacecraft relative motion dynamics models," *Journal of Guidance, Control, and Dynamics*, vol. 40, pp. 1837–1859, 2017.

[25] S. D'Amico, "Autonomous formation flying in low earth orbit," Ph.D. dissertation, Delft University of Technology, 2010.

[26] A. Midas, "Using a curvilinear coordinate system for satellite relative motion," Master's thesis, Virginia Tech, 2024.

[27] C. A, "Über die anzahl der wurzeln einer algebraischen gleichung in einem kreise," *Mathematische Zeitschrift*, vol. 14, pp. 110––148, 1926.

[28] G. Cardano, T. Witmer, and O. Ore, *The Rules of Algebra: Ars Magna*, ser. Alianza Universidad. Dover Publications, 2007.

[29] C. H. Davis, *The Binary Search Algorithm*. Wiley, 1969, vol. 20, pp. 167–167.

[30] D. Vallado, P. Crawford, R. Hujsak, and T. Kelso, *Revisiting Spacetrack Report #3*.